Original article

Near-infrared smart responsive orthopedic implants with synergistic antimicrobial and bone integration-promoting properties

Ziming Liao [a,1], Luyao Zhang [a,1], Jingxuan Li [a], Yujie Zhou [a], Yu Cao [a], Yan Wei [a,b], Jingjing Du [c], Li Lu [d,*], Di Huang [a,b,**]

[a] Research Center for Nano-Biomaterials & Regenerative Medicine, Department of Biomedical Engineering, College of Biomedical Engineering, Taiyuan University of Technology, Taiyuan, 030024, PR China
[b] Shanxi-Zheda Institute of Advanced Materials and Chemical Engineering, Taiyuan, 030032, PR China
[c] Analytical & Testing Center, Hainan University, Haikou, 570228, PR China
[d] Department of Orthopaedics, Shanxi Key Laboratory of Bone and Soft Tissue Injury Repair, The Second Hospital of Shanxi Medical University, Taiyuan, 030001, PR China

ABSTRACT

Background: The decline in antibiotic use has made the treatment of post-implant infections increasingly challenging, especially the problem of bacterial invasion caused by inadequate tissue fusion with the implant in the early stages of the implant. Developing multiple methods to reduce bacterial infections through synergies will be superior to a single model of antimicrobial means.
Methods: The composite coating composed of titanium phosphate (TiP)/copper oxide nanoparticles (CuO)/nano-hydroxyapatite (n-HA) named TiP-ua was used to kill *Staphylococcus aureus* (*S. aureus*) and *Escherichia coli* (*E. coli*) under near infrared (NIR) irradiation by means of photothermal therapy (PTT) and photodynamic therapy (PDT) synergism.
Results: The TiP-ua composite coating can reach about 60 °C and produce a certain amount of reactive oxygen species after 15 min irradiation with 980 nm near infrared light with 0.9 W/cm^2 power. Under the NIR irradiation of 0.9 W/cm^2 power for 10 min, the composite coating can achieve about 90% killing effect on *S. aureus* and more than 90% killing effect on *E. coli*. In terms of mouse pre-osteoblasts (MC3T3-E1), TiP-ua showed more superiority in promoting osteogenic differentiation ability. In the mouse infection model, it also showed good antibacterial effect, and could significantly reduce the expression of inflammatory factors and accelerate wound healing. In the bone defect model, the intervention significantly accelerated the regeneration of neobone tissue and enhanced osseointegration capacity.
Conclusions: The experimental results show that TiP-ua coating not only has good photothermal conversion ability, but also has good biosafety, which can accelerate the regeneration and repair of bone tissue around the implant, including accelerating the osteogenic differentiation of cells, and reduce the activity of bacteria to effectively reduce the inflammatory response.
The translational potential of this article: The collaborative antibacterial and bone repair coating in this study has a simple preparation process, high repeatability, high biosafety and positive effect on bone tissue repair, and has great clinical application potential in orthopedics and dental implants.

1. Introduction

Titanium (Ti) orthopedic implants are commonly used to replace missing bone and restore normal function [1]. Compared to the hydrogel implants that researchers have promoted in recent years, titanium implants will show better support [2]. However, Ti implants are

---

* Corresponding author.
** Corresponding author. Research Center for Nano-Biomaterials & Regenerative Medicine, Department of Biomedical Engineering, College of Biomedical Engineering, Taiyuan University of Technology, Taiyuan, 030024, PR China.
E-mail addresses: liludoc@163.com (L. Lu), huangjw2067@163.com (D. Huang).
[1] These authors contributed equally to this work.

susceptible to bacterial infection during the implant placement process due to their inherent lack of antimicrobial and anti-infective properties, which can lead to implant placement failure [3]. Common antimicrobial orthopedic implant means include reducing bacterial adsorption [4,5], contact antimicrobial [6] and release of antimicrobial particles for sterilization [7,8]. However, for bacteria that are already adsorbed to the implant surface, means of reducing their adsorption become meaningless. Also contact antimicrobial, although good for bacterial killing, is detrimental to the integration of normal tissues. The bactericidal mode of releasing antimicrobial particles is only effective at the beginning of the implantation period, and as the implantation time increases, the number of antimicrobial particles decreases and the bacterial control decreases. In addition, the use of antibiotic drugs is also commonly used in clinical antibacterial and anti-infection treatment, with the frequent use of drug resistance bacteria will seriously affect health [9,10]. Therefore, there is an urgent need for a long-lasting, controlled, and safe antimicrobial method.

Recently, there has been interest in the development of smart responsive near infrared (NIR) orthopedic implants to address these challenges [11]. NIR-responsive orthopedic implants are designed to have an impact on the prevention and treatment of bacterial infections using phototherapeutic techniques such as photodynamic therapy (PDT) or photothermal therapy (PTT) [12]. In addition, some NIR-responsive orthopedic implants contain materials that promote bone tissue repair, leading to faster and more effective osseointegration. The use of NIR-responsive implants has the potential to improve the long-term success of implants by reducing the risk of infection and promoting bone tissue repair [13]. This technology is still in the early stages of development and currently common photocatalytic photothermal materials such as MXene [14], metal sulfide [15–17] and Ti dioxide [18] are available. But more research is focused on its antibacterial and anti-infection ability. In fact, the same attention needs to be paid to the osteoblastic differentiation capacity of cells and the rate of bone tissue repair, and more research is needed to fully understand their potential advantages and limitations. In conclusion, the NIR-responsive implant is an innovative technology that is expected to improve the success rate of implant surgery, and its PDT production of reactive oxygen species and synergistic effect with PTT will be able to long-acting kill bacteria safely. TiP not only has good ability to promote cell osteogenic differentiation and accelerate bone integration, but also has excellent biocompatibility [19]. Moreover, studies of TiP as a photothermal coating to kill bacteria in vivo are very rare.

In this study, the nanoflower-like titanium phosphate (TiP) coating was prepared on the surface of a Ti substrate to demonstrate that this coating is a highly efficient photothermal conversion coating. The TiP coating was then hydrothermally loaded with homogeneous copper oxide nanoparticles to enhance its NIR-responsive effect, and finally the nano-hydroxyapatite (n-HA) coating was further induced by calcification to cover the copper oxide nanoparticles to form a composite coating (TiP/CuO/n-HA named TiP-ua). In vitro studies demonstrated that the composite TiP-ua coating exhibits excellent antibacterial properties through the synergistic effects of PDT and PTT. Under NIR irradiation, the TiP-ua coating maintained a high level of biosafety. Furthermore, the micro-nano surface topography of the coating significantly reduced cellular inflammatory responses. In vivo experiments further confirmed the superior performance of TiP-ua-coated implants, which exhibited remarkable antibacterial efficacy and effectively mitigated inflammatory responses. Consistent results were observed in a bone defect model, where TiP-ua implants promoted accelerated bone regeneration and improved osseointegration capabilities. These findings highlight the potential of TiP-ua implants in addressing persistent implant-associated infections and propose a novel method for clinical applications in orthopedic and dental implantology.

2. Experimental

2.1. Material and methods

(1) Material

Anhydrous, ethanol hydrogen peroxide and hexamethyltetramine were obtained from Tianjin Tianli Chemical Reagents Co., Ltd., China. Phosphate was purchased from Tianjin Yongda Chemical Reagents Co., Ltd. Titanium was bought from Jinfu Equipment manufacturing Co., Ltd. Anhydrous calcium chloride, and anhydrous copper sulfate were obtained from Shanghai Taitan Technology Co., Ltd.

(2) Preparation of TiP coating

In order to make the Ti sheet dust-free and oil-free, the Ti sheet was cleaned by ultrasonic alternately in deionized water and alcohol for 30 min, and the samples were dried after cleaning. The samples were then placed vertically in a PTFE-lined reactor, and a solution consisting of 8.5 wt% phosphoric acid and 9 wt% hydrogen peroxide was poured into the reactor to react at 0.15 MPa and 120 °C for 24 h. After hydrothermal reaction, rinse with deionized water and dry at 50 °C.

(3) Preparation of TiP-Cu coating

0.002 g $Cu(CO_2CH_3)_2 \cdot H_2O$ was mixed with 10 mL deionized water and placed in a 200 °C PTFE lined reactor for 1 h. The samples treated by the above method were labeled as TiP-Cu. The sample was removed from the solution, washed off the floating matter that was not firmly bonded on the surface, and put in a drying oven with blast air at 50 °C for drying.

(4) Preparation of TiP-Ca coating

The TiP was placed vertically in a reactor lined with PTFE solution at 120 °C for 1 h. The solution consisted of 1 M $CaCl_2$ and 0.701 g $C_6H_{12}N_4$ and was dried in a blast drying oven at 50 °C for later use.

(5) Preparation of TiP-ua coating

TiP-Cu was placed vertically in a reactor with PTFE and reacted with the internal solution at 120 °C for 1 h. The solution consisted of 1 M $CaCl_2$ and 0.701 g $C_6H_{12}N_4$. Samples were taken out and rinsed with deionized water, and then dried in an air blast drying oven at 50 °C.

2.2. Characterization

The surface morphology of the samples was observed using scanning electron microscope (SEM, JSM-7100F, Japan). The elemental composition on the surface of the samples was observed using Energy-dispersive X-ray spectroscopy (EDS, Oxford Max^N, UK). The crystal structure was examined by X-ray diffraction (XRD, X'Pert PRO, The Netherlands) in a step scan mode with a step size of 0.02° ranging from 10° to 80°. The determine their chemical compositions by using the Fourier transform infrared (FTIR, Bruker Alpha, Germany). The contact angle (CA) test of various samples was determined by the VAC apparatus (AST products, Inc., US).

2.3. Photothermal effects

The photothermal performance test was carried out under NIR light at 980 nm. The samples were put into a 24 well plate, and 1 mL PBS was added into each hole to irradiate in turn under NIR light with a power of 0.9 W/cm^2. The real-time temperature of different samples in different time periods was detected and recorded with a thermal imager, and the thermal imaging of the samples was taken.

2.4. Detection of reactive oxygen species (ROS)

The active oxygen species formation of the samples were detected under 980 nm NIR light (0.9 W/cm^2) to evaluate the photodynamic properties of the samples. Pure Ti was used as a control. Singlet oxygen ($^1O_2$) was detected by DPBF and generated in different samples under 980 nm laser (0.9 W/cm^2). The sample was immersed in 3 mL DPBF medium (ethanol solution) and then exposed to 980 nm laser for 0, 1, 3, 6, 9 min. After the reaction, the absorbance of DPBF solution was measured by ultraviolet spectrometer at 414 nm.

2.5. In vitro antibacterial properties

Before the antibacterial experiment, the Ti, TiP, TiP-Cu, TiP-Ca and TiP-ua coating samples were autoclaved and prepared in triplicate for each condition. The sterilized solid medium was removed from the oven and inverted. About 20 mL of solid medium was poured into each dish and left to cool. The sterilized samples were placed in 24 well plates, and 1 mL bacterial suspension with a concentration of 1×10^5 colony forming units (CFU)/mL was added to each sample. The power densities were 0.6 W/cm^2, 0.9 W/cm^2, 1.2 W/cm^2 and 1.5 W/cm^2 when the samples were irradiated with 980 nm NIR light for 10 min. After the treatment, 20 μL bacterial solution was taken on the medium for CFU analysis, and then the culture dish was placed upside down in a 37 °C incubator for 24 h, and the number of colonies was taken out, photographed, and measured. The formula for calculating the antibacterial rate is R = $[(\lambda_0 - \lambda_t)/\lambda_0] \times 100\%$, where R is the antibacterial rate (%), λ_0 is the average number of viable bacteria on the control sample, λ_t is the average number of viable bacteria on Ti, TiP, TiP-Cu, TiP-Ca and TiP-ua under NIR light illumination. The unirradiated blank group was the control group.

2.6. Protein leakage

To quantitative the protein concentration of bacteria, the *Staphylococcus aureus* (*S. aureus*) and *Escherichia coli* (*E. coli*) were placed in 1 mL bacterial suspension (1×10^5 CFU/mL). After treatment with 980 nm NIR light (0.9 W/cm^2), the bacteria of different samples were collected and centrifuged at 13,000 rpm for 4 min at 4 °C. The supernatants were harvested, and the protein leakage of each group was monitored by the BCA Protein Assay Kit (Beyotime, China) on a microplate reader.

2.7. Biocompatibility assessment

2.7.1. Cell proliferation and adhesion

Mouse pre-osteoblasts (MC3T3-E1) were employed to evaluate the cell proliferation and adhesion on different samples. The samples were disinfected by high-pressure steam sterilization and then placed in 24 well plates. Afterwards, the cells were seeded on the surfaces of the samples at a density of 5×10^3/mL and incubated at 37 °C in an incubator containing 5% CO$_2$. The cells were cultured for 1, 4, and 7 days for the proliferation assay and 1 day for the attachment assay. The Cell Counting Kit (CCK)-8 (Beyotime, China) was used to analyze cell proliferation. At each time point of measurement, 1 mL of medium was added to each well with 100 μL CCK-8 reagent according to the manufacturer's instructions. After 1 h incubation at 37 °C, the absorbance was read with a microplate reader (Biorad iMark, USA) at 450 nm. Each group included three parallel samples. The samples cultured for 1 days were rinsed with phosphate-buffered saline (PBS), fixed with 2.5% glutaraldehyde (Aladdin, China), and dehydrated by sequential soaking in 30%, 50%, 75%, 80%, 95%, and 100% ethanol for 15 min each. Then the dried samples were observed under SEM.

2.7.2. Live/dead fluorescent staining

The biocompatibility of all samples was evaluated by measuring the cell viability of MC3T3-E1 contacted with the surface coating. The cells

on TiP and TiP-Ca coated samples were analyzed with the live/dead assay by staining with Calcein-AM and EthD-1, and pure Ti samples were used as the control. MC3T3-E1 cells (density 5×10^3/mL) were suspended in culture medium then seeded on samples so that the coating directly contacted the cells to examine potentially toxic effects. After they were incubated for 1, 4, and 7 days in an incubator containing 5% CO$_2$ at 37 °C, the medium was removed, and each sample was washed with PBS. Subsequently, the samples were dyed in PBS solution containing 2 μM Calcein-AM and 2 μM EthD-1 for 30 min in the dark. The fluorescent images were recorded by an inverted fluorescent microscope (Eclipse Ti-S, Nikon, Japan).

2.7.3. Cell structure observation (NIR/No NIR)

After the cells were co-cultured with the material for 24 h, the medium was sucked out, washed twice with PBS, and then 1 mL PBS was added. After 10 min irradiation of each sample with 980 nm NIR light, PBS was sucked out and nuclear and membrane staining was performed. The observation was recorded by inverted fluorescence microscope.

#### 2.7.4. In vitro inflammation evaluation

Macrophages were seeded in 24 well plates at a density of 40% and cultured for 24 h, after which the medium was replaced with RAW264.7-specific culture medium. The materials were then introduced, and an inflammatory model was induced by adding LPS at a concentration of 1 μg/mL, followed by overnight incubation. After three washes with PBS, the cells were fixed with immunostaining fixative for 15 min and subsequently washed three times with PBS. Permeabilization was performed using 1% Triton X-100, followed by overnight blocking with immunostaining blocking buffer. The cells were then incubated overnight with diluted primary antibodies, including anti-TNF-α rabbit and anti-iNOS rabbit. After three PBS washes, the samples were incubated with Cy3-labeled goat anti-rabbit IgG secondary antibody at room temperature for 2 h. Finally, the nuclei were counterstained with DAPI for 5 min, followed by three PBS washes. The samples were then observed and statistically analyzed.

2.7.5. Alkaline phosphatase (ALP) activity

ALP activity was determined by quantifying the amount of phosphoric p-nitrophenol (pNPP), a product of alkaline phosphatase reactions, using an ALP kit (Beyotime) according to assay protocols. 1 mL cell suspension was inoculated on each sample in a 24 well plate at a density of 5×10^3/mL. After 7 days and 14 days, the culture medium was removed, and the samples were washed with PBS. Then, 200 μL cell lysis solution (Beyotime) was added to each well for 4 min. Collect the lysate and centrifuge and take the supernatant. 50 μL supernatant was added into the 96 well plate and incubated with 50 μL pNPP at 37 °C for 30 min. Finally, 100 μL termination solution was added and the optical density was measured using an enzyme-labeled meter set at 405 nm. A calibration curve was obtained using a solution of p-nitrophenol of known concentration. The unit of diethanolamine (DEA) enzyme activity is calculated according to the definition in the ALP Kit instruction manual.

2.8. Immunofluorescent staining

Immunocytochemistry analysis was carried out to explore the osteogenic differentiation of MC3T3-E1 cells after 7 days and 14 days culture with the samples. Briefly, the samples were washed with PBS three times, fixed with 4 % (v/v) paraformaldehyde (PFA, Biosharp, China) for 15 min, and washed gently three times with PBS. After that, the cells were blocked using PBS containing 0.3% (v/v) Triton X-100 (Solarbio, China) and 5% (v/v) goat serum (Absin, China) overnight at 4 °C. Then the fixed cells were incubated overnight at 4 °C with the respective primary antibody: rabbit polyclonal anti-osteocalcin (1: 200 (v/v), Beyotime, China) or rabbit monoclonal anti-Runt-related transcription factor 2 (1: 200 (v/v), Beyotime, China). After incubation time, the
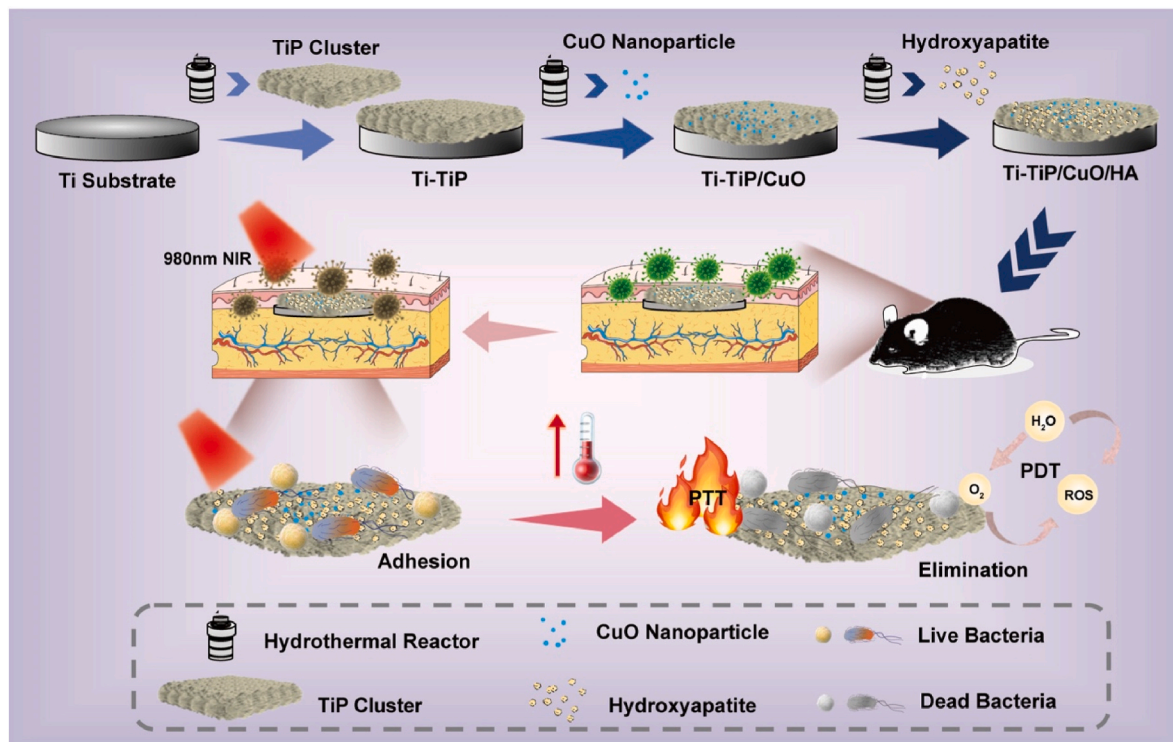
Scheme 1. Schematic illustration of the NIR-responsive Ti-TiP/CuO/HA (TiP-ua) coating for synergistic effects on the implant-related infection. The TiP-ua coating construct by hydrothermal. TiP clusters were constructed in situ on the surface of Ti, and then CuO nanoparticles were loaded on the TiP surface. Finally, n-HA was formed in situ by PO_4^{3-} groups from TiP. At mild temperatures, the high thermal action responsive by NIR significantly enhanced the antibacterial activity of the TiP-ua composite coating, resulting in a large amount of dispersion and penetration on the surface of the Ti implant, and killing bacteria through a synergistic antibacterial strategy of PTT and PDT. The TiP-ua composite coating also showed good biocompatibility and anti-infection effect in rats while synergizing antibacterial activity under NIR.

samples were washed with PBS three times each for 5 min and were incubated with the secondary antibody (Cy3-labeled Goat Anti-Rabbit IgG, 1 : 400 (v/v), Beyotime, China and Goat Anti-Rabbit IgG-Alexa Fluor 488, 1 : 400 (v/v), Beyotime, China) for 2 h at room temperature. After rinsing with PBS, the cell nuclei were counterstained with DAPI (Bevotime, China). Finally, the samples were rinsed with PBS and observed by the inverted fluorescence microscope. The whole process was carried out under darkness. The fluorescence intensity of osteocalcin (OCN) and Runt-related transcription factor 2 (RUNX2) were calculated using Image J software.

2.9. In vivo antibacterial evaluation

All animal procedures in the experiments were performed in accordance with the Guidelines for Care and Use of Laboratory Animals of Taiyuan University of Technology and approved by the Animal Ethics Committee of Taiyuan University of Technology (TYUT-202208010). Male C57 rats (4 weeks) were divided into 5 groups: (1) Ti, (2) TiP, (3) TiP-Cu, (4) TiP-Ca, (5) TiP-ua. Each group has three rats. The different samples were subcutaneously embedded into the back site of corresponding rats. And *S. aureus* (10 μL, 2×10^5 CFU mL^{-1}) was injected into the injured area. After surgery, the wound sites of rats were sutured. After 20 min post-surgery, the groups (1)–(5) were irradiated with 980 nm laser (0.9 W/cm^2) for 5 min, respectively. Taking real-time thermal photographs of different populations under near-infrared irradiation. After 7 days, the rats were sacrificed and the samples of each group were separated into Luria–Bertani medium and ultrasonic shocked (180 W, 37 °C) for 5 min for collecting the *S. aureus* on the surface of the implant. Furthermore, the bacterial colonies of each group were quantified by diluted plate assay after culturing 1 day at 37 °C.

2.10. Histology evaluation

The surrounding tissues of different samples were fixed in 4% PFA solution for staining. All staining figures were accustomed to assessing the anti-infected efficiency of different modified samples in vivo. The histological analysis of different samples was observed via a light microscope.

2.11. In vivo bone defect repair evaluation

2.11.1. Animal models

10 randomized SD rat were allocated into five groups: Ti, TiP, TiP-Cu, TiP-Ca, and TiP-ua. All animals were anesthetized with 3% sodium pentobarbital after one week of acclimatization. The rat's skin was fully exposed, and a lateral knee incision approximately 2 cm in length was made. Soft tissues were bluntly separated up to the lateral epicondyle of the femur utilizing vascular forceps. An electric drill was used to create a bone defect (1 mm), which was thoroughly rinsed with saline before implanting the different implant groups. The skin was sutured layer by layer, and the incision was sterilized with povidone-iodine. Postoperatively, penicillin was administered intramuscularly for three days. 4 and 8 weeks post-surgery, the rat were euthanized and specimens of the femur were collected. The specimens were stored in a 4% PFA solution for subsequent experiments.

2.11.2. Micro-CT

The harvested specimens were fixed and preserved in a 4% PFA solution to maintain structural integrity. Subsequently, the femoral samples were subjected to Micro-CT imaging, utilizing a multilevel thresholding algorithm to accurately differentiate bone tissue from surrounding soft tissues. Quantitative analysis focused on key
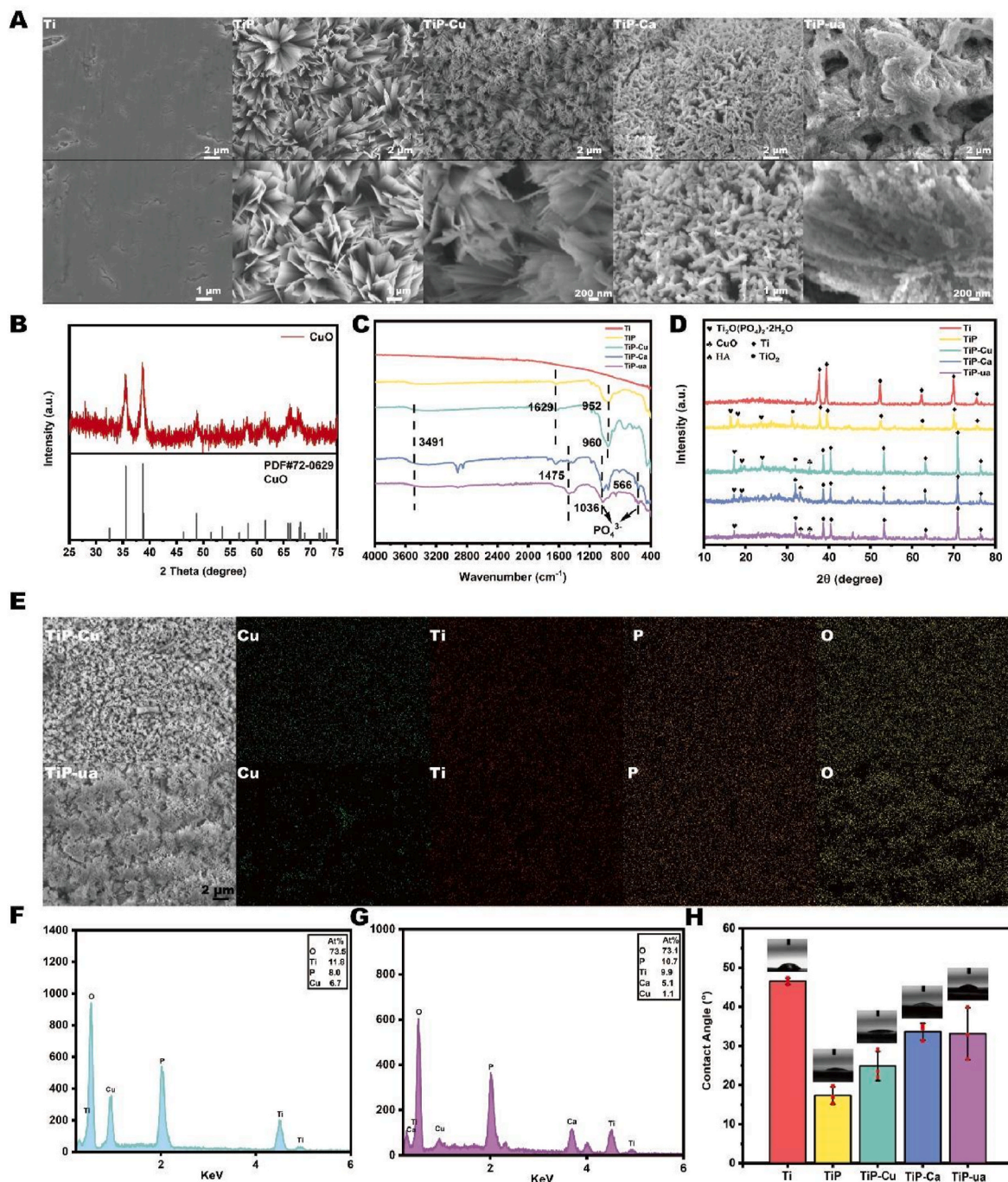
Fig. 1. The preparation and morphological characterization of different modified coatings. (A) SEM of Ti, TiP, TiP-Cu, TiP-Ca and TiP-ua coatings; (B) XRD image of surface CuO in TiP-Cu; (C) FTIR spectra of the samples; (D) The XRD patterns of the sample; (E) Elemental maps of TiP-Cu and TiP-ua; (F) EDS spectrum of the TiP-Cu coating; (G) EDS spectrum of the TiP–ua coating; (H) Water contact angles on various sample surfaces.

parameters, including implant positioning accuracy, potential implant migration or subsidence, and osteogenic performance metrics such as bone volume to total volume ratio (BV/TV) and trabecular thickness (Tb.Th).

2.11.3. Histological evaluation

To evaluate osseous development inside the implant across various groups, the specimens were preserved in 4% PFA solution and then dehydrated using a gradient of 70%, 95%, and 100% ethanol. The femurs were embedded in methyl methacrylate solution and stained after paraffin embedding. The specimens with implant were sectioned using a hard tissue slicer. HE staining was employed to examine bone repair

around the implants, and Masson staining was performed to observe bone tissue maturation around the implants.

2.11.4. Immunohistochemistry

Bone tissues were preserved in 4% PFA solution and then transferred to 10% EDTA decalcification solution (20–30 times the tissue volume) for decalcification. Specimens were thoroughly washed, and endogenous peroxidase in the bone tissues was inactivated using hydrogen peroxide. Following routine dehydration, embedding, and sectioning, the specimens were kept overnight at 4 °C with antibodies against RUNX2 (an osteogenic marker) and IL-6 (an inflammation marker). Secondary antibodies were then applied, and the samples were
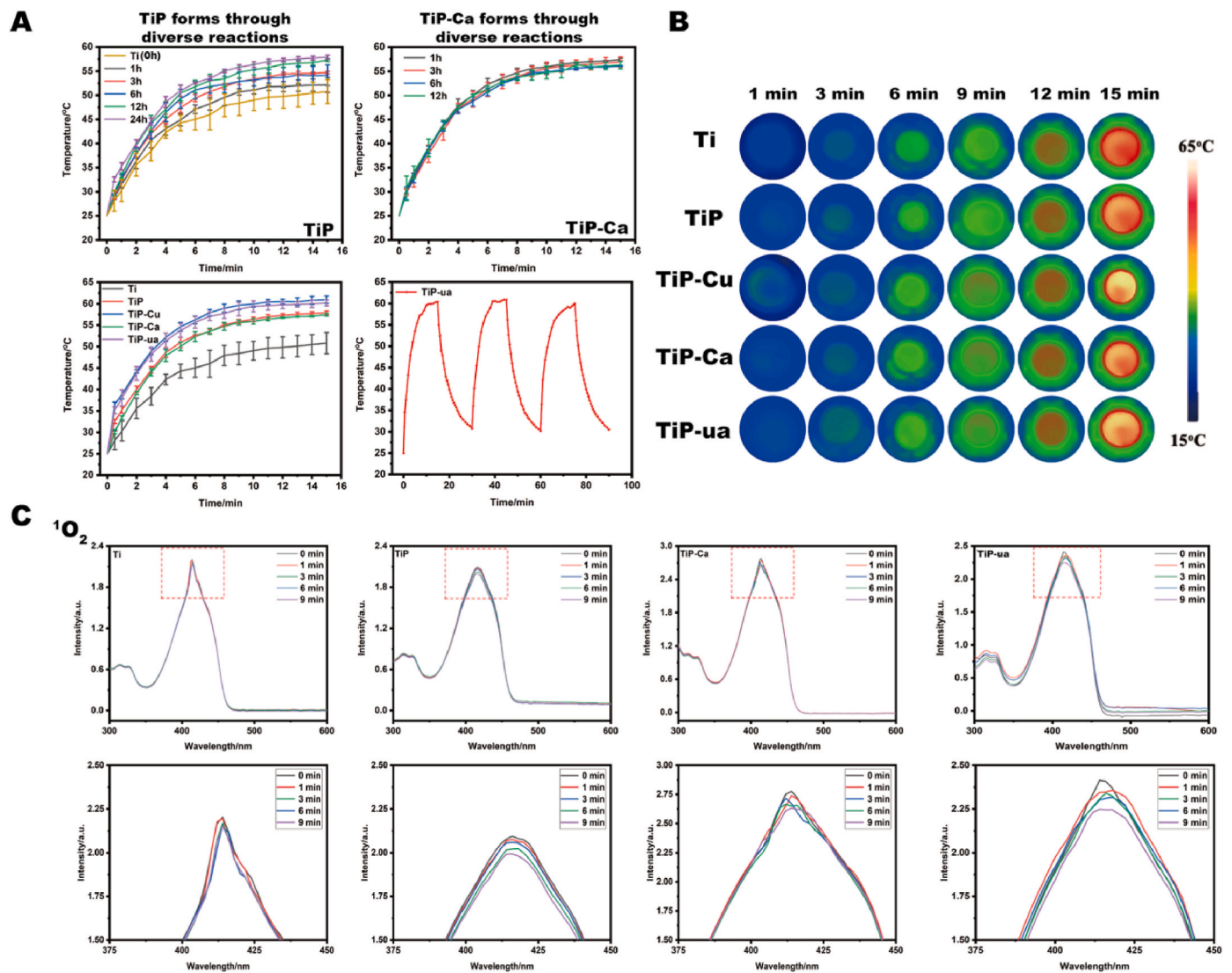
Fig. 2. The photothermal properties of different modified coatings. (A) TiP temperature curve in PBS at different reaction times, the temperature curve of TiP-Ca in PBS at different reaction times, temperature curves of different samples in PBS and the temperature rise and fall curve of TiP-ua in PBS when illumination is "on-off" (power = 0.9W/cm^2); (B) Images for infrared thermal imaging of different samples; (C) Detection of ROS upon irradiation with 980 nm NIR light at 0.9 W/cm^2 for 9 min: $^1O_2$ are detected from the decay of DPBF of different samples.

visualized.

2.11.5. In vivo safety evaluation

In vivo safety of implant was evaluated in SD rat. The venous blood and different organs (heart, liver, spleen, lung and kidney) were collected. The analysis of routine blood biomarkers was performed using a veterinary automated hematology analyzer (BC-2800vet, Mindray, China). Hematoxylin-eosin (HE) staining were conducted on heart, liver, spleen, lung and kidney to analyze histological damage.

2.12. Statistical analysis

A two-tailed analysis of variance (ANOVA) and t test were used to analyze significant differences between two groups of samples. Comparisons involving more than two groups were conducted using one-way ANOVA with a post hoc test. All experiments were repeated 3 times and expressed as mean ± standard deviation. SPSS 11.0 software was used for statistical analysis of the data with different significance levels. (*p < 0.05, **p < 0.01 and ***p < 0.001 were regarded as significant, highly significant, and extremely significant, respectively.).

3. Result and discussion

3.1. Synthesis and characterization

In this work, we designed an intelligent NIR-responsive antibacterial active Ti surface where CuO NPs and n-HA are incorporated with TiP cluster, achieving the multiple antibacterial therapeutic efficacies. The nano-photothermal agents CuO NPs [20] can improve NIR light energy into PTT and PDT, which can regulate the disassembly of bacterial as shown in Scheme 1.

Fig. 1A shows the surface morphology of the TiP coating after the first hydrothermal reaction, the flake structure is uniformly distributed on the substrate, increasing the area and surface roughness of the original Ti substrate, and the loading of the TiP coating surface with small particulate matter, proven by XRD analysis in Fig. 1B–be CuO nanoparticles to enhance the photothermal conversion of the coating [21]. The SEM figures also show the morphology of the TiP coating surface loaded with HA, compared to TiP-ua where the gaps between the coatings become smaller and the number of particles loaded becomes larger when the TiP coating surface loaded with CuO nanoparticles first.
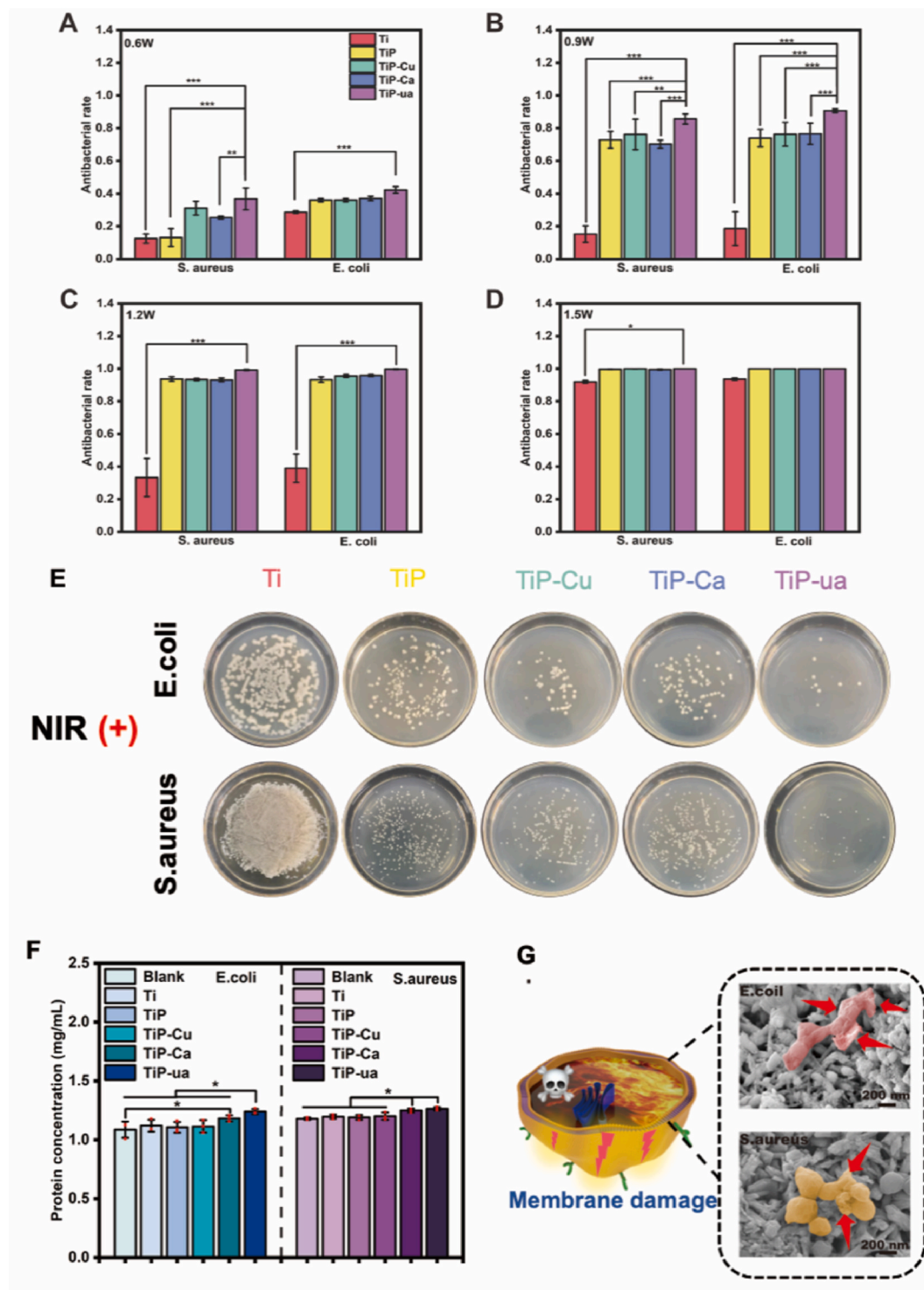
Fig. 3. Antibacterial activity of different samples against *S. aureus* and *E. coli*. (A–D) Antibacterial efficiency under different power treatment for 10 min (A) 0.6 W/cm^2; (B) 0.9 W/cm^2; (C) 1.2 W/cm^2; (D) 1.5 W/cm^2. (E) Number of *E. coli* and *S. aureus* colonies of the different samples with NIR irradiation were irradiated with 0.9 W/cm^2 NIR light for 10 min (F) Protein leakage of *E. coli* and *S. aureus* after 10 min treatment with 0.9 W/cm^2; (G) The SEM images of *E. coli* and *S. aureus* were processed with pseudo color. The red arrows point to the damage of cell membranes. (*p < 0.05, **p < 0.01, ***p < 0.001)

Fig. 1C shows the infrared diffraction images of different samples. It can be clearly seen that 952 cm^{-1} is the characteristic absorption peak of phosphoric acid group [22]. After adding CuO, the infrared diffraction peak shifts and the characteristic peak of phosphoric acid moves to 960 cm^{-1}. 566 cm^{-1} and 1036 cm^{-1} are the peaks of characteristic phosphoric acid of HA [23]. The peak at 3491 cm^{-1} is the characteristic peak of hydroxyl group [24]. The TiP-Cu sample may have the characteristic

peak of hydroxyl group due to the formation of part of Cu(OH)$_2$ in the reaction process of CuO, while the characteristic peak of hydroxyl group is more obvious in TiP-Ca due to the presence of HA. However, the surface of TiP-ua is covered by a layer of CuO nanoparticles, so the amount of HA coating after calcification is less than that without CuO particles, so the performance of hydroxyl characteristic peaks is not as obvious as that of TiP-Ca coating. It can also be seen from the XRD
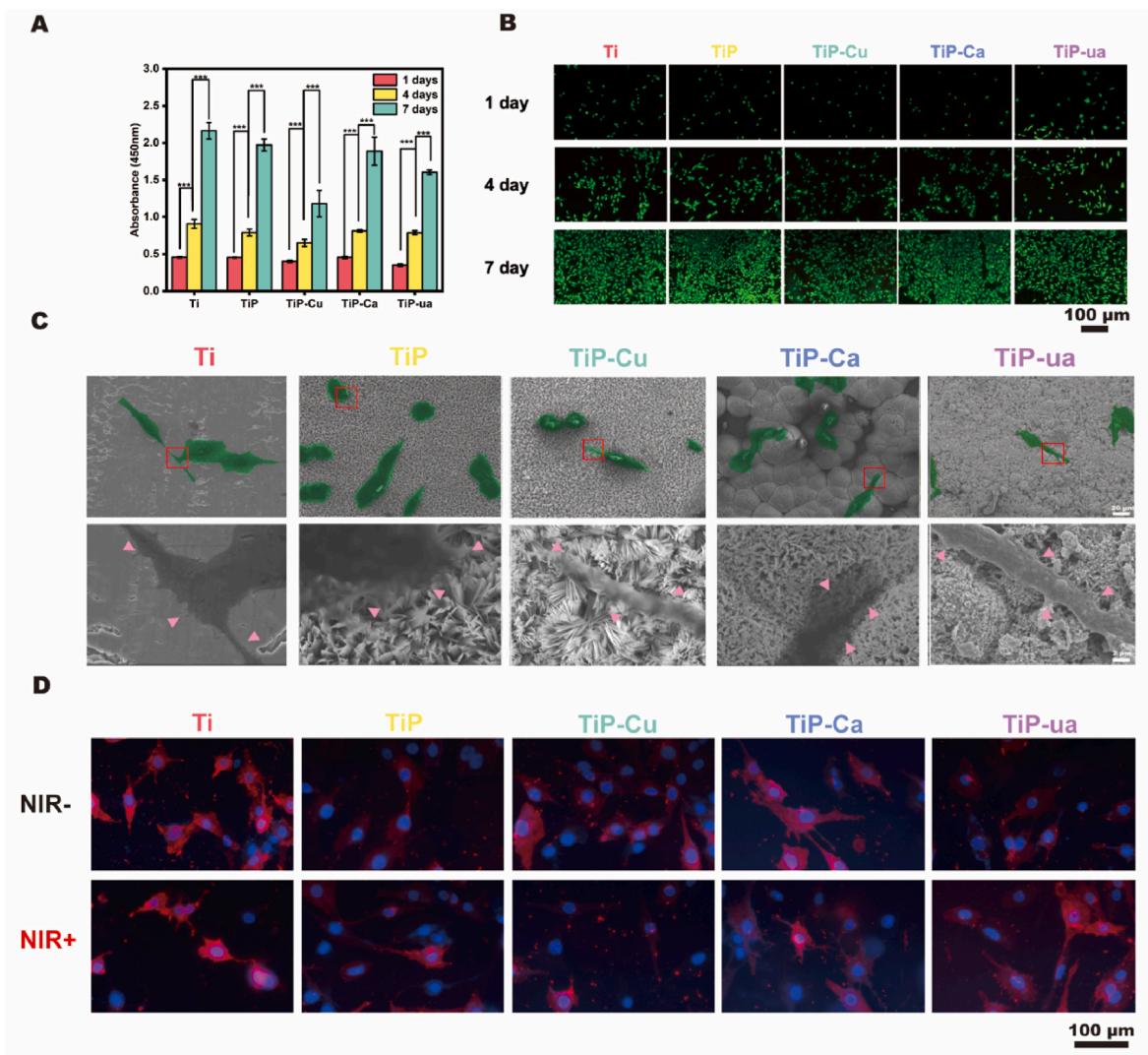
Fig. 4. In vitro biocompatibility of different samples. (A) The proliferation of MC3T3-E1 cells cultured on different samples for 1, 4 and 7 days was determined by CCK-8; (B) Fluorescent images with live/dead staining; (C) SEM images and high-magnification images of MC3T3-E1 cells cultured on samples for 1 day; (D) Nuclear membrane staining images of MC3T3-E1 cells after 24 h without or with NIR light. (***p < 0.001).

images in Fig. 1D that TiP, TiP-Ca and TiP-ua samples generated by treated Ti will have some TiO_2 on the sample surface due to the use of H_2O_2 in the preparation process. After the hydrothermal treatment of synthesized CuO, the characteristic peak of CuO can be obviously observed on the sample surface. The peaks of HA (PDF No. 73–1731) are also observed on the material surface after calcification, demonstrating successful introduction of HA to the material surface through calcification. Compared with TiP-Ca samples, the HA peak of TiP-ua samples decreased, because the content of HA in TiP-ua is less than that in TiP-Ca, which is consistent with the results shown in the previous FTIR.

The surface elemental composition of both TiP-Cu and TiP-ua samples was analyzed by EDS surface scanning, as shown in Fig. 1E, F and G. TiP-Cu coating successfully introduce Cu element on the surface of TiP. After calcification the Cu element content is reduced due to the formation of a new HA coating on the surface effectively reducing the cytotoxic effect of CuO due to direct contact with cells or organization [25]. And enhances the biocompatibility of the implants.

The values of contact angles (CA) between all samples and water are shown in Fig. 1H. The CA values of Ti, TiP, TiP-Cu, TiP-Ca and TiP-ua are 46.5 ± 0.8°, 17.3 ± 2.2°, 24.9 ± 3.7°, 33.6 ± 2.1° and 33.1 ± 6.7°, respectively. Ti is the worst hydrophilic, the CA of TiP-Cu is slightly greater than that of TiP, and the CA of TiP-ua is substantially less than

that of TiP-Cu. Different surface physicochemical structures result in different hydrophilicity [26].

3.2. Light-to-heat conversion

In order to find the most suitable photothermal conversion ability of TiP-ua coating under 980 nm NIR light irradiation, the thermal imager was used to detect temperature changes and draw the temperature curve. As shown in Fig. 2A, the photothermal conversion performance with 980 nm NIR of TiP was investigated. It can be clearly seen that the photothermal conversion efficiency of TiP increases with the extension of reaction time. The TiP prepared for 24 h can reach more than 55 °C after 15 min irradiation with NIR light. Fig. 2A also shows the photothermal conversion ability of TiP-Ca samples with different preparation times. Contrary to TiP's conclusion, the photothermal conversion efficiency of TiP-Ca decreases with the extension of preparation time. We believe that in addition to the inherent optical ability of TiP, the flower-like nanostructure also makes an important contribution to the photothermal effect [27], and the nanostructure can improve the transfer heat performance and promote the photothermal conversion [28,29], while the granular HA coating formed by consuming TiP does not have this ability. Therefore, in order to prepare TiP-ua coatings with the most
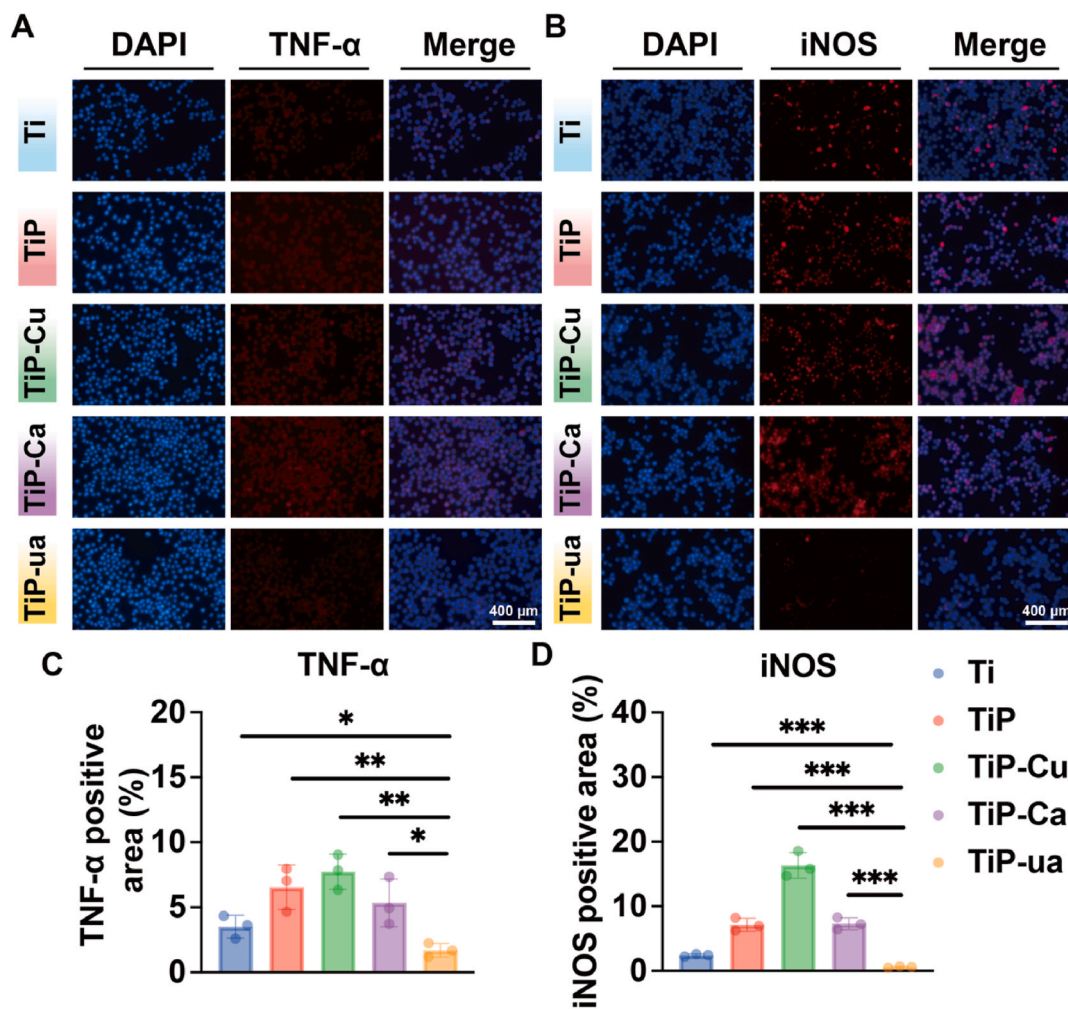
Fig. 5. In vitro anti-inflammatory of different samples. (A) Representative fluorescence images of TNF-α; (B) Representative fluorescence images of iNOS; (C) The quantitative analysis of the fluorescence images of TNF-α; (D) The quantitative analysis of the fluorescence images of iNOS.

suitable photothermal conversion efficiency, TiP fabricated for 24 h and TiP-Ca fabricated for 1 h are selected as the best preparation parameters for subsequent experiments. Fig. 2A also shows the photothermal conversion efficiency of different samples under the most suitable preparation parameters. It is obvious that the nanoflower-like TiP structure can increase the photothermal conversion ability of Ti and the addition of CuO nanoparticles has the same ability. Both TiP-ua and TiP-Cu samples can reach about 60 °C when irradiated with 980 nm NIR for 15 min. TiP-ua can maintain good photothermal stability under cyclic irradiation test. Fig. 2B directly shows the change of the surface temperature of TiP-ua samples with the change of irradiation time. The image appears blue-green when the irradiation time is 1 min, and bright white when the irradiated time is 15 min, indicating the excellent photothermal conversion ability of the material.

In order to study the photocatalytic performance of different samples with NIR light, DPBF was used to measure the content of $^1O_2$ produced by NIR irradiation. The intensity of absorption peak decreased with the increase of the content of $^1O_2$ produced. As shown in Fig. 2C, TiP-ua exhibits the maximum absorption peak intensity change after 9 min irradiation with 0.9 W/cm^2 NIR, while Ti has the smallest change. It can be concluded that TiP-ua has the best photocatalytic ability compared with the other three types of samples.

3.3. NIR-responsive bacteria eradication performance of modified coating in vitro

The antibacterial activity of Ti, TiP, TiP-Cu, TiP-Ca and TiP-ua against *S. aureus* and *E. coli* was determined by a spread plate method at different power levels. For *S. aureus* at 0.6 W/cm^2 the power is too low to kill the bacteria effectively. At 0.9 W/cm^2 TiP-ua shows the best antibacterial activity and the antibacterial rate is about 90%. At 1.2 W/cm^2 and 1.5 W/cm^2 TiP-ua show a significant difference in antibacterial power only with Ti, probably because the power is too high and the surface temperature is too high, it has a significant effect on the bacteria. For *E. coli* 0.6 W/cm^2 is not enough to make a significant difference between TiP-ua and the other samples except for Ti, because the power was too low for the PTT and PDT advantages to be realised. 0.9 W/cm^2 was sufficient for TiP-ua to kill *E. coli*, and 1.2 W/cm^2 and 1.5 W/cm^2 showed similar trends to *S. aureus*. Overall, at 0.9 W/cm^2, the TiP-ua sample showed excellent PTT and PDT antibacterial activity, unlike the other samples, and was able to kill most bacteria and it is no concern about damage to normal cells. Fig. 3E shows the direct view of the antibacterial effect of different samples with 0.9 W/cm^2 NIR by spread plate method. The degree of bacterial membrane damage is measured by the situation of protein leakage as shown in Fig. 3F. The protein leakage of TiP-ua is the most serious in *E. coli*, and the protein leakage of TiP-Ca and TiP-ua is the most serious in *S. aureus*. The increased protein content in the solution indicates the increased permeability of the bacterial membrane and the higher the degree of damage of the bacterial
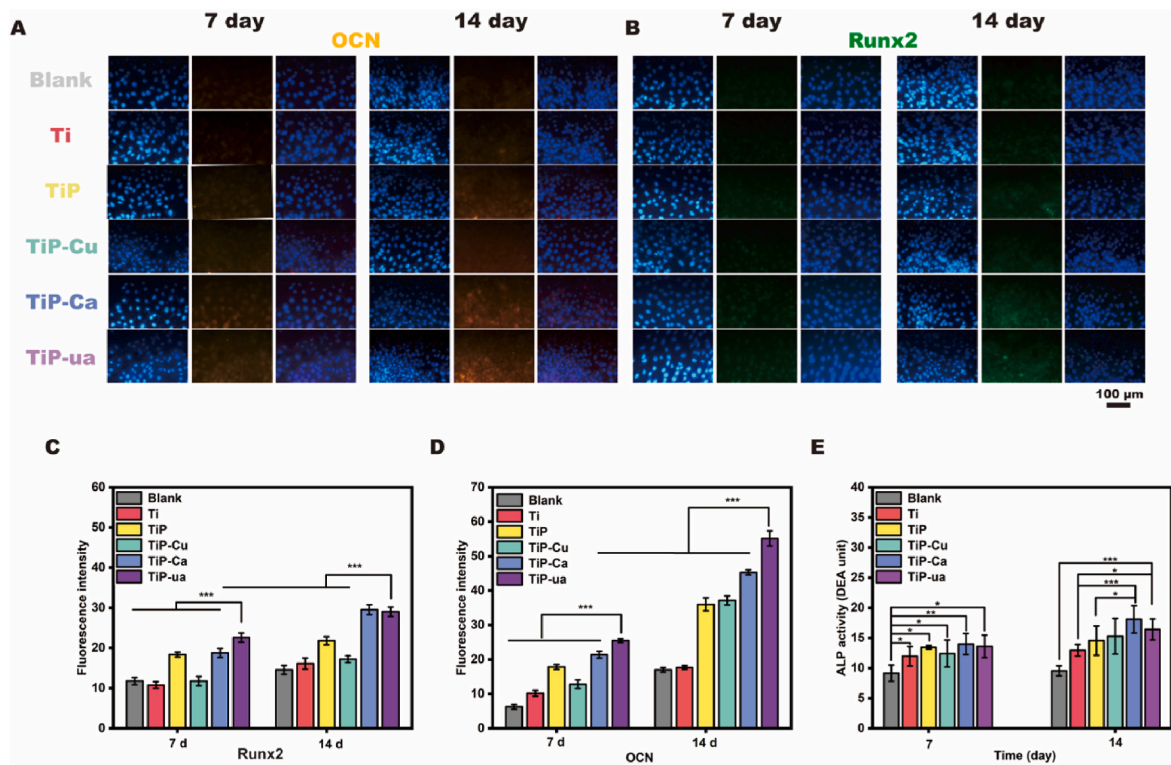
Fig. 6. In vitro osteogenic ability of different samples. (A and B) Immunofluorescent images of OCN and RUNX2 expressed by MC3T3-E1 cells cultured with samples for 7 and 14 days; (C and D) Fluorescence intensity analysis of RUNX2 and OCN of different samples after 7 and 14 days; (E) The ALP activity of MC3T3-E1 cells cultured for 7 and 14 days. (*p < 0.05, **p < 0.01, ***p < 0.001).

membrane [30]. Microscopic observations in Fig. 3G show that the bacterial membrane structure of *E. coli* and *S. aureus* (as indicated by the red arrow) has been damaged to varying degrees, which further indicates that TiP-ua can effectively destroy the bacterial membrane and kill bacteria under the combined action of PTT and PDT.

3.4. In vitro biocompatibility, osteogenesis and anti-inflammatory of implant

The cell biological response of the material was assessed by measuring the proliferation of MC3T3-E1 osteoblasts on the surface of the samples and the data is shown in Fig. 4A. After the cells were co-cultured with the material for 1, 4 and 7 days, the number of cells in each group increase with increasing days of cultivation and all had good proliferation, indicating that all samples are non-cytotoxic and biocompatible. The TiP-Cu group has less cell proliferation than the other groups to some extent because the CuO nanoparticles generated on the surface are in direct contact with the cells [31]. However, TiP-ua does not show a clear advantage in promoting cell proliferation, possibly because the role of HA and TiP are to promote cell directed differentiation, while it does not show a clear advantage in promoting cell proliferation, resulting in a disadvantage in the total number of cells [32,33]. The cytotoxicity of the samples was assessed using live/dead staining as shown in Fig. 4B. The results show that the number of cells on the surface of the samples increase as the culture time increased and little cell death is observed, consistent with the previous CCK-8 results indicating that all materials are non-cytotoxic and biocompatible. Fig. 4C shows that the SEM pictures of MC3T3-E1 cells. It is found that cells spread state in 1 day. All the samples show good biocompatibility.

To further evaluate whether the normal cell structure would be disrupted under NIR light (0.9W/cm^2) irradiation conditions, MC3T3-E1 cells grown for 24 h was subjected to NIR light irradiation and stained for nuclei and membranes. The results show that all samples

without NIR light irradiation have good cell structure and the cell membranes do not show any obvious breakage or deformation. In the condition of NIR light (0.9W/cm^2) irradiation, the cells on TiP and Ti can maintain good morphology, and most of the cell membranes in the TiP-Cu are damaged and the nuclei were exposed, while after the introduction of HA coating (TiP-ua), the situation of TiP-Cu is improved, the TiP-ua could clearly be seen to have the same intact cell structure as the cells under no NIR light conditions, and there is no obvious destruction of the cell membranes, therefore we conclude that the irradiation of TiP-ua with NIR light (0.9W/cm^2) for 10 min does not disrupt the normal cell structure and has a good biosafety.

To elucidate the regulatory effects of different implants on the functional phenotype of macrophages in vitro, we co-cultured macrophages with various samples and induced inflammatory responses using lipopolysaccharide (LPS) stimulation for 12 h. As shown in Fig. 5A, immunofluorescence analysis revealed a significant increase in the proportion of TNF-α-positive macrophages following LPS stimulation. Notably, the TiP-ua group exhibited the smallest fluorescence area (Fig. 5C), indicating the lowest level of TNF-α expression. Similarly, immunofluorescence analysis of iNOS (Fig. 5B) demonstrated analogous trends, with TiP-ua showing the weakest fluorescence signal (Fig. 5D), suggesting minimal iNOS expression. The observed results may be attributed to the ability of TiP-ua to attenuate the ROS generation associated with TiP-Cu, thereby mitigating cellular inflammatory responses. Additionally, the finely structured micro-nano surface topography of TiP-ua may contribute to the suppression of cellular inflammation, further enhancing its anti-inflammatory properties [34, 35].

After 7 and 14 days of MC3T3-E1 cells culture, the expressions of OCN and RUNX2 osteogenic proteins were studied by immunofluorescence staining. OCN fluoresces red, RUNX2 fluoresces green, and the nuclei are stained blue with DAPI. Immunofluorescence staining images as shown in Fig. 6A and B shows that after 7 days of cultivation, OCN
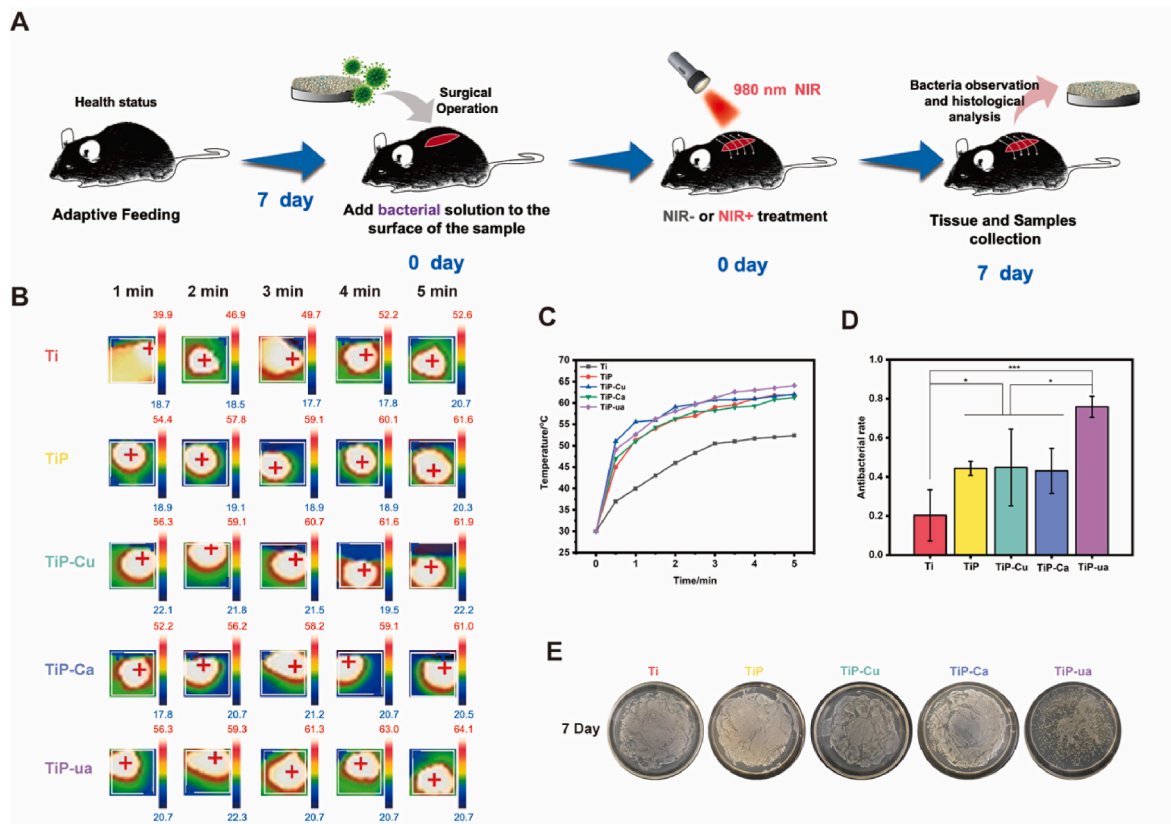
Fig. 7. In vivo antibacterial effect of different samples. (A) Schematic illustration of the experimental process for *S. aureus* infected implants in model rats; (B, C) Thermal photographs of real-time temperature and corresponding photothermal heating curve of different groups with NIR irradiation in vivo (Irradiation intensity: 0.9 W/cm^2, 5 min); (D) The antibacterial rate of the implant samples of different group; (E) Number of *S. aureus* colonies of the implant samples for different groups with NIR irradiation. (*P $<$ 0.05, ***p $<$ 0.001).

fluorescence is more obvious in the samples of TiP, TiP-Ca and TiP-ua groups, and the fluorescence intensity of each group is improved after 14 days of cultivation compared with 7 days of cultivation. The fluorescence intensity of OCN in TiP-Ca and TiP-ua groups increase most obviously and the fluorescence expression is the highest. In addition, the fluorescence expression of RUNX2 at 7 day is relatively obvious in TiP, TiP-Ca and TiP-ua groups. The change of fluorescence intensity is less than that in OCN after 14 days of culture, but the fluorescence expression of TiP-ua and TiP-Ca groups is higher in all RUNX2 groups.

Further calculation results by Image J software shown in Fig. 6C and D. The fluorescence expression of TiP-ua at 7 days of RUNX2 is the highest among the other 4 groups. Although the fluorescence intensity of TiP-ua at 14 days is slightly lower than that of TiP-Ca group, there is no significant difference, and TiP-Ca and TiP-ua show significant differences with other groups. The fluorescence intensity of TiP-ua group in OCN at 7 days is significantly higher than that of the other 4 groups and TiP-ua group have the same result at 14 days. At the same time, TiP-ua exhibited the largest OCN fluorescence intensity of all groups at 14 days. These results indicate that TiP-ua coating can effectively promote the high expression of cell related osteogenic differentiation protein, accelerate the osteogenic differentiation of cells, and facilitate the rapid bone repair. The ALP assays illustrate that the induced ALP activity variation is not obvious from sample to sample in 7 days, the ALP activity of samples is only significantly higher than the blank. But at the 14 days the ALP activity of TiP-Ca and TiP-ua are significantly higher than the blank and Ti samples. And TiP-Ca is also significantly higher than that of TiP. These results indicate that the preparation of HA induce the increase of ALP activity to a certain extent, enhance the ability of composite coating to induce osteogenic differentiation, and accelerate bone tissue regeneration and repair.

3.5. NIR-responsive bacteria eradication performance of modified coating in vivo

Considering excellent bacteria eradication performance, the antibacterial efficacy of the modified coating in vivo was further investigated in an animal model with subcutaneous infections (Fig. 7A). Due to the susceptibility of the soft tissue seal and epithelial barrier, the soft tissue around the Ti-based implants (such as percutaneous implant and orthopedic implant) can be easily infected by bacteria, thereby increasing the implant failure and related complications [36]. Therefore, the subcutaneous implant infection model was applied to investigate the antibacterial effect of the modified coatings. Briefly, the samples contaminated with *S. aureus* were implanted subcutaneously into the back of rats. After implantation, a certain amount of *S. aureus* suspension was injected into the back wound of rats and the wound was sutured in time to simulate implant associated infection. As shown in Fig. 7B, the subcutaneous samples are irradiated with 980 nm NIR light (0.9 W/cm^2) for 5 min respectively, the representative temperature images and the local NIR-responsive real-time temperature changes of the implant sites for different groups are detected by the thermal camera. As shown in Fig. 7C, the temperature of TiP-ua group growth rapidly from 30 °C to 64.1 °C after irradiation for 5 min, whereas only a slight temperature change from 30 °C to 52.6 °C of Ti group. However, the temperature of TiP is rapidly increased and stabilize at about 61.6 °C, as similar as that of TiP-Cu to 61.9 °C, and the TiP-Ca is rapidly to 61.0 °C proving the efficiently photothermal conversion capability in vivo.

After taking out the stitches at 7 days post-surgery, the infection site of different groups was harvested to evaluate their antibacterial capacity in vivo. To quantify the residue *S. aureus* around the samples, the modified samples were collected separately into sterile PBS for CFU
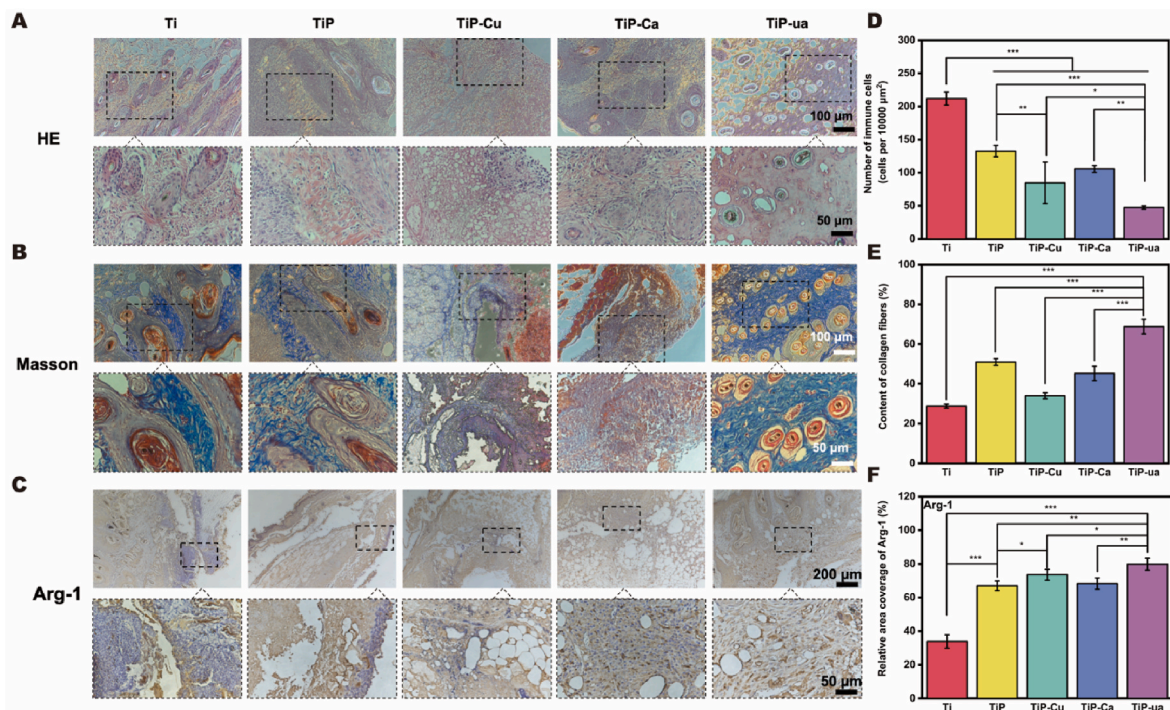
Fig. 8. In vivo demonstration of different coatings promoting infectious tissue healing under NIR irradiation. Histological evaluation by HE (A) and Masson (B) staining of the soft tissues around the modified samples with NIR irradiation; IHC staining images of the soft tissues around the modified samples harvested from rats for positive cells of Arg-1; (C) Quantitative evaluation of inflammatory cells (D) and collagen formation (E) of different modified samples calculated from HE and Masson staining; Quantitative analysis of IHC staining intensity of Arg-1; (F) based on the images. (*p < 0.05, **p < 0.01, ***p < 0.001).

assay. Upon 980 nm NIR irradiation, all experimental groups show a CFU decreasing at different degrees. As shown in Fig. 7D, the TiP-ua group displayed a prominent antibacterial efficiency of 75.9 % against *S. aureus* on coating surfaces which is significantly higher than the other groups (Ti: 20.3 %, TiP: 44.3 %, TiP-Cu: 44.9 %, TiP-Ca: 43.1 %). The representative images of spread plates of viable *S. aureus* on samples for TiP-ua reveal a remarkable decrease in comparison with other groups (Fig. 7E). The results demonstrate that the *S. aureus* on TiP-ua implant could be efficiently eliminate by the NIR-responsive PTT antibacterial strategy.

Researchers have found that the surrounding tissues of exogenous implants are prone to infection in the early postoperative period [37]. Bacteria contaminated with implants can induce host immune response, causing an inflammatory response involving immune cells and a clotting cascade [38]. During implant infection, the accumulation of bacteria around the implant can be a persistent virulence factor, leading to the accumulation of large numbers of inflammatory cells, degradation of collagen, and sustained damage to surrounding tissues [39]. Therefore, hematoxylin-eosin staining (HE) and Masson staining were used to evaluate the inflammation and recovery of the tissue surrounding the modified sample. As shown in Fig. 8A and D, many inflammatory cells are found in the tissues of the control group Ti, indicating that the severe bacterial infection cause an obvious immune response. However, most of the cells in TiP-ua group have normal morphology, with only a few neutrophils dotted, indicating a slight inflammatory response in vivo. At the same time, disease-related pathogens can destroy collagen-containing tissues by producing collagenase and collagen-degrading enzymes [40]. Regeneration of collagen fibres are an important part of wound healing. The Masson staining results in Fig. 8B are further used to illustrate the significant differences in the recovery of infected tissues in different groups. A large area of regular and uniform collagen fibres are found in the TiP-ua group, indicating abundant cell migration and formation of extracellular matrix and granulation tissue [41]. As shown in Fig. 8E, the deposition level of blue collagen fibres in

TiP-ua group are significantly higher than that in control Ti group and other modified coating groups, indicating that TiP-ua group has good tissue regeneration ability.

Pathogenic bacteria can induce acute immune response, leading to massive accumulation of immune cells, suppurative inflammation and severe damage to surrounding tissues [39]. In the occurrence and development of bacterial infectious diseases, inflammatory response is the physiological response of the body to stimulation, usually mediated by inflammatory cytokines. As a heterogeneous immune cell, macrophages can differentiate into pro-inflammatory M1 and anti-inflammatory M2 phenotypes under different microenvironments [42]. The anti-inflammatory factor Arg-1 of macrophages plays a key role in the formation and repair of infected tissues [43]. In order to further investigate the anti-inflammatory properties of different coatings, the expression of typical M2-related anti-inflammatory factor Arg-1 was analyzed using the immunohistochemical (IHC) results of the soft tissues surrounding the modified samples. As shown in Fig. 8C and F, anti-inflammatory cytokine levels of Arg-1 are significantly increased in the NIR irradiated TiP-ua coating compared to the other groups, indicating outstanding inflammatory regulatory or regenerative properties. Balanced expression of anti-inflammatory factors in infected tissues, including enhanced polarization of macrophages M2, suggests a potential inflammatory regulatory effect of NIR radiation on TiP-ua coatings. Combined with the above results, the TiP-ua coating responsive by NIR has excellent antibacterial ability, which can resist bacterial invasion and inhibit the inflammatory response of infected tissues during the recovery process.

3.6. The in vivo bone defect repair capacity of the modified coating

To further evaluate the osteogenic potential of the samples in bone defect repair, critical-sized femoral defects were created in a rat model and implanted with different materials [44]. After 4 and 8 weeks of implantation, the defect sites were harvested for comprehensive
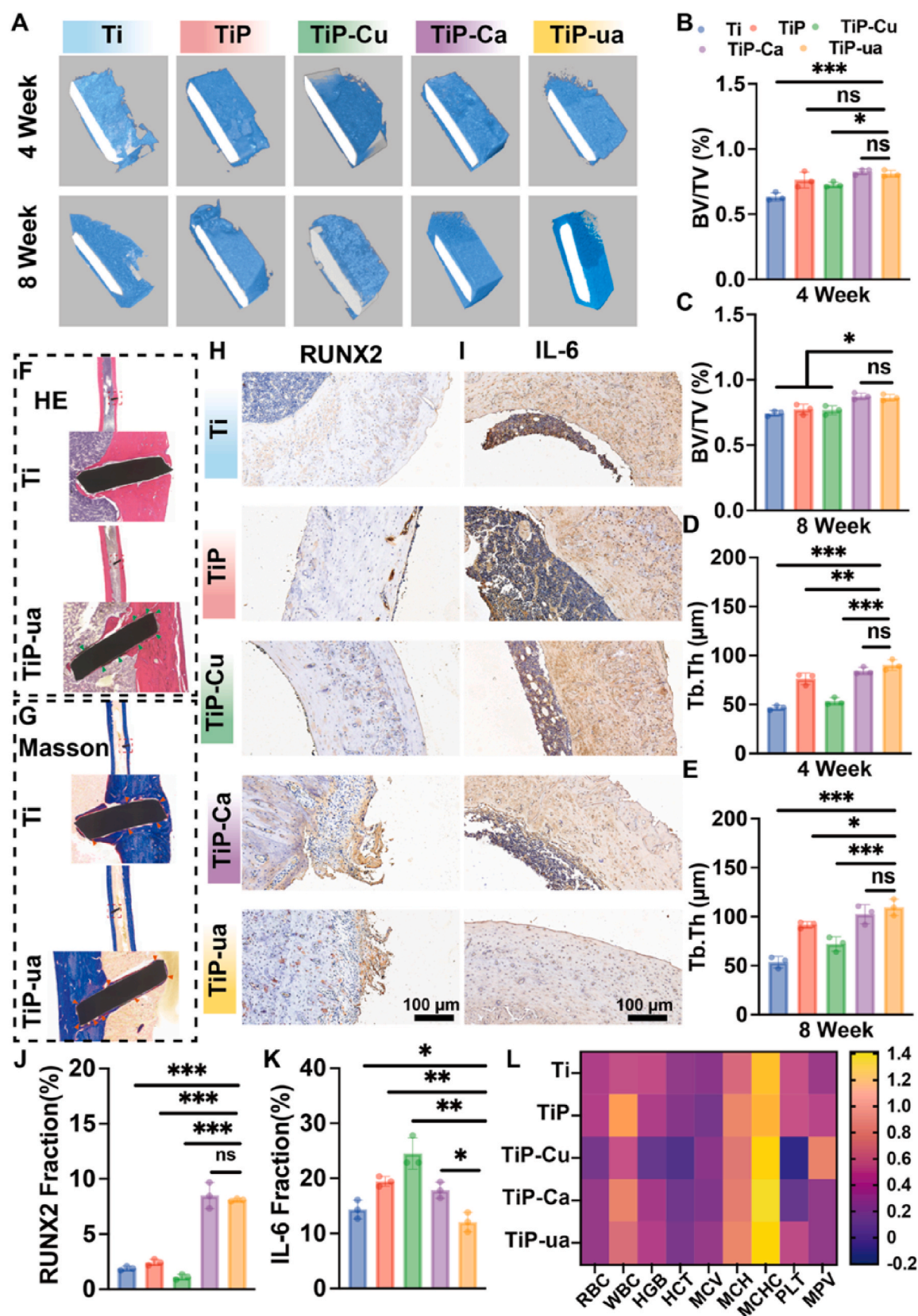
Fig. 9. In vivo bone regeneration. (A) The representative 3D reconstructed Micro-computed tomography (Micro-CT) scanning images of regenerated bone tissue induced by different samples; (B–E) Quantitative morphometric analysis of the bone volume/total volume (BV/TV) and trabecular thickness (Tb. Th) of the newly formed bone using micro-CT analysis; (F) The He staining of Ti and TiP-ua implants (8 weeks); (G) The Masson staining of Ti and TiP-ua implants (8 weeks); (H) The immunohistochemical staining of RUNX2 (4 weeks); (I) The immunohistochemical staining of IL-6 (4 weeks); (J) Quantitative analysis of RUNX2; (K) Quantitative analysis of RUNX2; (L) The complete blood count of different samples.
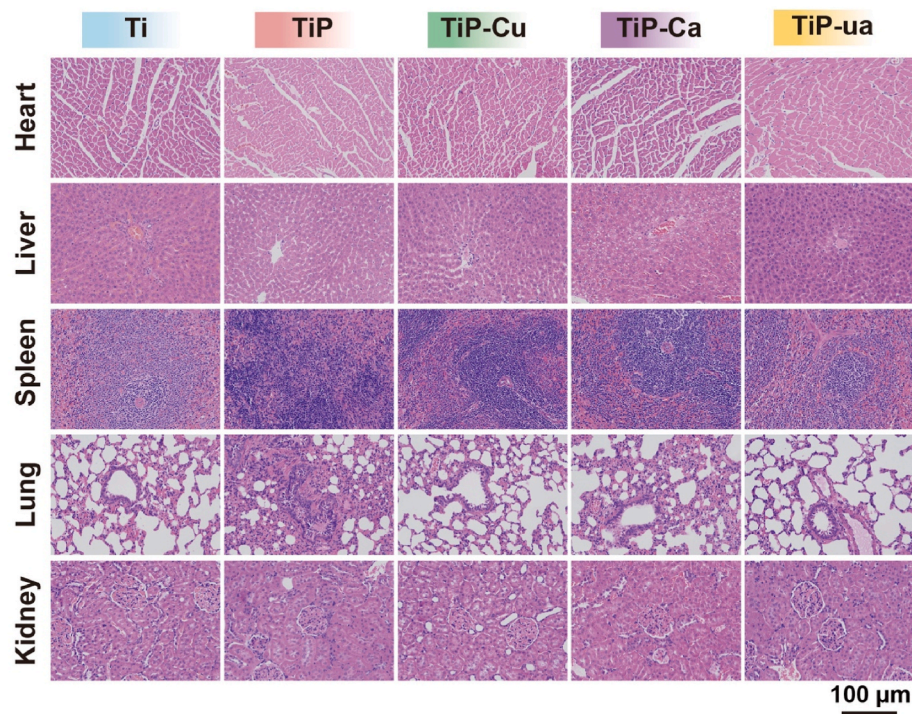
Fig. 10. In vivo biocompatibility of the different implants. Representative HE staining images of major (heart, liver, spleen, lung and kidney) organs.

analysis. Micro-CT scanning revealed distinct osteogenic patterns among the five groups (Fig. 9A). At the 4 weeks, Ti and TiP-Cu groups exhibited significant implant exposure with incomplete osseointegration, while TiP showed relatively complete coverage but with localized areas of thin new bone formation. Notably, TiP-Ca and TiP-ua demonstrated superior osteogenic performance, with the most substantial new bone formation. This trend persisted at 8 weeks, with TiP-Ca and TiP-ua showing more complete bone coverage and higher bone mineral density [45].

Quantitative analysis of micro-CT data (Fig. 9B and C) revealed that TiP-ua significantly increased the BV/TV ratio compared to pure Ti and TiP-Cu at both time points. Although TiP-Ca showed comparable parameters to TiP-ua due to their similar hydroxyapatite structures, no significant difference was observed between these two groups. Analysis of trabecular thickness (Fig. 9D and E) demonstrated that TiP-ua significantly enhanced trabecular thickness compared to Ti, TiP, and TiP-Cu, indicating higher maturity of the newly formed bone and superior bone repair capacity.

Histological evaluation through H&E and Masson's trichrome staining (Figs. 9F and 8G) revealed reduced inflammatory cell infiltration and enhanced bone-implant contact in the TiP-ua group compared to Ti controls, suggesting improved implant stability and osseointegration [46]. Immunohistochemical analysis of RUNX2 expression (Fig. 9H) demonstrated significantly larger positive areas in the TiP-ua group compared to other groups (Fig. 9J), indicating enhanced osteogenic differentiation. Conversely, IL-6 staining (Fig. 9I) revealed minimal positive areas in the TiP-ua group (Fig. 9K), suggesting the lowest inflammatory response among all groups.

Although TiP-Ca demonstrated comparable bone repair capacity to TiP-ua, its clinical applicability may be limited by inferior antibacterial properties and potential inflammatory risks. To further assess biosafety, we conducted complete blood count analysis and histopathological examination of major organs (heart, liver, spleen, lungs and kidneys). As shown in Fig. 10, all experimental groups showed no significant inflammatory cell infiltration or pathological changes, confirming the excellent biocompatibility of TiP-ua without inducing significant local

or systemic inflammatory responses or immune rejection [47]. These systematic evaluations demonstrate the safety, reliability, and significant clinical potential of TiP-ua material for bone defect repair applications.

4. Conclusions

In summary, a uniform TiP flower cluster coating was successfully formed on the surface of Ti substrate, with CuO and HA nanoparticles in situ deposited on the TiP surface. The TiP-ua coating not only demonstrated excellent photothermal performance under 980 nm NIR laser irradiation but also exhibited superior synergistic antibacterial effects through combined PTT and PDT, effectively eradicating both Gram-positive *S. aureus* and Gram-negative *E. coli*, thereby achieving controllable and enhanced antibacterial treatment. Importantly, the TiP-ua coating exhibited excellent biosafety. Beyond its robust antibacterial activity, it effectively suppressed inflammation in an in vivo infection model while promoting more mature neobone formation, enhanced osseointegration, and reduced inflammatory responses during bone defect repair. In a word, the TiP-ua coating, as an effective strategy for synergistic antibacterial therapy, provides a promising approach for antibacterial infection prevention and repair in medical implant coatings. The NIR-responsive TiP-ua coating is expected to further expand the application of PTT and PDT assisted antibacterial-repair strategies in the biomedical field [48].

CRediT authorship contribution statement

Ziming Liao: Conceptualization, Writing – review & editing, Writing – original draft. **Luyao Zhang:** Investigation. **Jingxuan Li:** Investigation. **Yujie Zhou:** Investigation. **Yu Cao:** Investigation. **Yan Wei:** Investigation. **Jingjing Du:** Investigation. **Li Lu:** Supervision. **Di Huang:** Conceptualization, Supervision, Project administration, Writing – review & editing, Writing – original draft.

Declaration of competing interest

References

[1] Zhao Y, Sun YH, Lan WW, Wang Z, Zhang Y, Huang D, et al. Self-assembled nanosheets on NiTi alloy facilitate endothelial cell function and manipulate macrophage immune response. J Mater Sci Technol 2021;78:110–20.

[2] Schwab A, Wesdorp AM, Xu J, Abinzano F, Loebel C, Falandt M, et al. Modulating design parameters to drive cell invasion into hydrogels for osteochondral tissue formation. J Orthop Translat 2023;41:42–53.

[3] Guo C, Cui W, Wang X, Lu X, Zhang L, Li X, et al. Poly-l-lysine/Sodium alginate coating loading nanosilver for improving the antibacterial effect and inducing mineralization of dental implants. ACS Omega 2020;5:10562–71.

[4] Bakhshandeh S, Amin Yavari S. Electrophoretic deposition: a versatile tool against biomaterial associated infections. J Mater Chem B 2018;6:1128–48.

[5] Spengler C, Nolle F, Mischo J, Faidt T, Grandthyll S, Thewes N, et al. Strength of bacterial adhesion on nanostructured surfaces quantified by substrate morphometry. Nanoscale 2019;11:19713–22.

[6] Fang Z, Chen J, Zhu Y, Hu G, Xin H, Guo K, et al. High-throughput screening and rational design of biofunctionalized surfaces with optimized biocompatibility and antimicrobial activity. Nat Commun 2021;12:3757–69.

[7] Wang X, Yan L, Ye T, Cheng R, Tian J, Ma C, et al. Osteogenic and antiseptic nanocoating by in situ chitosan regulated electrochemical deposition for promoting osseointegration. Mater Sci Eng C 2019;102:415–26.

[8] Karbowniczek J, Cordero-Arias L, Virtanen S, Misra SK, Valsami-Jones E, Tuchscherr L, et al. Electrophoretic deposition of organic/inorganic composite coatings containing ZnO nanoparticles exhibiting antibacterial properties. Mater Sci Eng C 2017;77:780–9.

[9] Xiong F, Wei S, Sheng H, Wu S, Liu Z, Cui W, et al. Three-layer core-shell structure of polypyrrole/polydopamine/poly(l-lactide) nanofibers for wound healing application. Int J Biol Macromol 2022;222:1948–62.

[10] Maleki A, He J, Bochani S, Nosrati V, Shahbazi MA, Guo B. Multifunctional photoactive hydrogels for wound healing acceleration. ACS Nano 2021;15: 18895–930.

[11] Li X, Tan Z, Guo B, Yu C, Yao M, Liang L, et al. Magnet-oriented hydrogels with mechanical–electrical anisotropy and photothermal antibacterial properties for wound repair and monitoring. Chem Eng J 2023;463:142387–400.

[12] Ma Y, Jiang L, Hu J, Yuan Y. Engineering a multiscale multifunctional theragenerative system for enhancing osteosarcoma therapy, bone regeneration and bacterial eradication. Chem Eng J 2022;430:132622–36.

[13] Wu Z, Tian Q, Wang J, Feng Y, Li L, Xu C, et al. A bone implant with NIR-responsiveness for eliminating osteosarcoma cells and promoting osteogenic differentiation of BMSCs. Colloids Surf B Biointerfaces 2022;211:112296–304.

[14] Yu J, Lao J, Chu D, Wang D, Tang D, Li D, et al. Reversible photodriven droplet motion on Ti$_3$C$_2$ MXene film for diverse liquids. ACS Appl Mater Interfaces 2020; 12:19194–200.

[15] Curcio A, De Walle AV, Benassai E, Serrano A, Luciani N, Menguy N, et al. Massive intracellular remodeling of CuS nanomaterials produces nontoxic bioengineered structures with preserved photothermal potential. ACS Nano 2021;15:9782–95.

[16] Gao Q, Zhang X, Yin W, Ma D, Xie C, Zheng L, et al. Functionalized MoS$_2$ nanovehicle with near-infrared laser-mediated nitric oxide release and photothermal Activities for advanced bacteria-infected wound therapy. Small 2018;14:e1802290–304.

[17] Li M, Li L, Su K, Liu X, Zhang T, Liang Y, et al. Highly effective and noninvasive near-infrared eradication of a Staphylococcus aureus biofilm on implants by a photoresponsive coating within 20 min. Adv Sci 2019;6:1900599–614.

[18] Pan JF, Yu XH, Dong JJ, Zhao L, Liu LL, Liu JL, et al. Diatom-inspired TiO$_2$-PANi-decorated bilayer photothermal foam for solar-driven clean water generation. ACS Appl Mater Interfaces 2021;13:58124–33.

[19] Liao ZM, Zhang LY, Lan WW, Du JJ, Hu YC, Wei Y, et al. In situ titanium phosphate formation on a titanium implant as ultrahigh bonding with nano-hydroxyapatite coating for rapid osseointegration. Biomater Sci 2023;11:2230–42.

[20] Liang CX, Li CT, Zhu YC, Du XY, Zeng YF, Zhou YH, et al. Light-driven photothermal catalysis for degradation of toluene on CuO/TiO$_2$ Composite:

[21] dominating photocatalysis and auxiliary thermalcatalysis. Appl Surf Sci 2022;601: 154144–54.

Shanmugam M, Kuthala N, Vankayala R, Chiang CS, Kong XY, Hwang KC. Multifunctional CuO/Cu$_2$O truncated nanocubes as trimodal image-guided near-infrared-III photothermal agents to combat multi-drug-resistant lung carcinoma. ACS Nano 2021;15:14404–18.

[22] Müller V, Balvay S, Gaillard C, Tadier S, Gremillard L, Djurado E. One-step fabrication of single-phase hydroxyapatite coatings on Ti-alloy implants by electrostatic spray deposition: from microstructural investigation to in vitro studies. Surf Coating Technol 2021;427:127805–16.

[23] Jiang J, Liu W, Xiong Z, Hu Y, Xiao J. Effects of biomimetic hydroxyapatite coatings on osteoimmunomodulation. Biomater Adv 2022;134:112640–55.

[24] He D, Zhang X, Liu P, Liu X, Chen X, Ma F, et al. Effect of hydrothermal treatment temperature on the hydroxyapatite coatings deposited by electrochemical method. Surf Coating Technol 2021;406:126656–62.

[25] Naz S, Gul A, Zia M, Javed R. Synthesis, biomedical applications, and toxicity of CuO nanoparticles. Appl Microbiol Biotechnol 2023;107:1039–61.

[26] Yuan X, Wang Y, Liu L, Dong H, Yang G. Hydrophilic tyrosine-based phenolic resin with micro-ripples morphology for marine antifouling application. Colloids Surf B Biointerfaces 2022;217:112672–9.

[27] Csizmadia T. Simulation of the reflectivity properties of microstructured titanium surface by ray tracing method. J Laser Micro Nanoeng 2015;10:210–5.

[28] Zhu J, Luo Y, Tian J, Li J, Gao X. Clustered ribbed-nanoneedle structured copper surfaces with high-efficiency dropwise condensation heat transfer performance. ACS Appl Mater Interfaces 2015;7:10660–5.

[29] Gong X, Gao X, Jiang L. Recent progress in bionic condensate microdrop self-propelling surfaces. Adv Mater 2017;29:1703002–15.

[30] Zhang GN, Wu ZZ, Yang YQ, Shi J, Lv J, Fang Y, et al. A multifunctional antibacterial coating on bone implants for osteosarcoma therapy and enhanced osteointegration. Chem Eng J 2022;428:131155–71.

[31] Gallo A, Manfra L, Boni R, Rotini A, Migliore L, Tosti E. Cytotoxicity and genotoxicity of CuO nanoparticles in sea urchin spermatozoa through oxidative stress. Environ Int 2018;118:325–33.

[32] Xu M, Liu T, Qin M, Cheng Y, Lan W, Niu X, et al. Bone-like hydroxyapatite anchored on alginate microspheres for bone regeneration. Carbohydr Polym 2022; 287:119330–41.

[33] Jiang N, Guo Z, Sun D, Ay B, Li Y, Yang Y, et al. Exploring the mechanism behind improved osteointegration of phosphorylated titanium implants with hierarchically structured topography. Colloids Surf B Biointerfaces 2019;184: 110520–8.

[34] Li YT, Yang CL, Yin XZ, Sun YH, Weng J, Zhou J, et al. Inflammatory responses to micro/nano-structured titanium surfaces with silver nanoparticles. J Mater Chem B 2019;7:3546–59.

[35] Dai H, Fan Q, Wang C. Recent applications of immunomodulatory biomaterials for disease immunotherapy. Explorations 2022;2:20210157.

[36] Fang J, Wan Y, Sun Y, Sun X, Qi M, Cheng S, et al. Near-infrared-activated nanohybrid coating with black phosphorus/zinc oxide for efficient biofilm eradication against implant-associated infections. Chem Eng J 2022;435: 134935–48.

[37] Osmon DR, Berbari EF, Berendt AR, Lew D, Zimmerli W, Steckelberg JM, et al. Infectious Diseases Society Of. Diagnosis and management of prosthetic joint infection: clinical practice guidelines by the Infectious Diseases Society of America. Clin Infect Dis 2013;56:18–55.

[38] Flemming HC, Wingender J. The biofilm matrix. Nat Rev Microbiol 2010;8: 623–33.

[39] Pestrak MJ, Chaney SB, Eggleston HC, Dellos-Nolan S, Dixit S, Mathew-Steiner SS, et al. Pseudomonas aeruginosa rugose small-colony variants evade host clearance, are hyper-inflammatory, and persist in multiple host environments. PLoS Pathog 2018;14:1006842–64.

[40] Krishnaswamy VR, Mintz D, Sagi I. Matrix metalloproteinases: the sculptors of chronic cutaneous wounds. Biochim Biophys Acta Mol Cell Res 2017;1864:2220–7.

[41] Brett D. A review of collagen and collagen-based wound dressings. Wounds U K 2008;20:347–56.

[42] Gu Q, Yang H, Shi Q. Macrophages and bone inflammation. J Orthop Translat 2017;10:86–93.

[43] Hager M, Cowland JB, Borregaard N. Neutrophil granules in health and disease. JAMA Intern Med 2010;268:25–34.

[44] Lin Z, Chen Z, Chen Y, Yang N, Shi J, Tang Z, et al. Hydrogenated silicene nanosheet functionalized scaffold enables immuno-bone remodeling. Explorations 2023;3:20220149.

[45] Zhao ZY, Ruan HT, Chen AP, Xiong W, Zhang MZ, Cai M, et al. Genetic engineered ultrasound-triggered injectable hydrogels for promoting bone reconstruction. Research-China 2023;6.

[46] Wang FQ, Ye YX, Zhang ZJ, Teng WSY, Sun HX, Chai XP, et al. PDGFR in PDGF-BB/PDGFR signaling pathway does orchestrates osteogenesis in a temporal manner. Research-China 2023;6.

[47] Liu LB, Liu HY, Lu XY, Yin ZS, Zhang W, Ye J, et al. Palladium-based nanocomposites remodel osteoporotic microenvironment by bone-targeted hydrogen enrichment and zincum repletion, vol. 7. Research-China; 2024.

[48] Liao Z, Liu T, Yao Z, Hu T, Ji X, Yao B. Harnessing stimuli-responsive biomaterials for advanced biomedical applications. Explorations 2025;5:20230133.